SUPPORTING INFORMATION:

Dissipative Quantum Tunneling Rates through the Incorporation of First-Principles Electronic Friction in Instanton Rate Theory II: Benchmarks and Applications

Y. Litman,[1, a)] E. S. Pós,[1] C. L. Box,[2] R. Martinazzo,[3] R. J. Maurer,[2] and M. Rossi[1, b)]

[1)] *MPI for the Structure and Dynamics of Matter, Luruper Chaussee 149, 22761 Hamburg, Germany*

[2)] *Department of Chemistry, University of Warwick, Coventry CV4 7AL, United Kingdom*

[3)] *Department of Chemistry, Università degli Studi di Milano, Via Golgi 19, 20133 Milano, Italy*

(Dated: 25 April 2022)

[a)] Electronic mail: yairlitman@gmail.com

[b)] Electronic mail: mariana.rossi@mpsd.mpg.de

I. CONVERGENCE OF INSTANTON CALCULATIONS

The convergence tests for the tunneling rates were performed using a 2x2x2 orthorhombic supercell containing four Pd atoms since it is expected to present similar convergence behavior as an 8x8x8 orthorhombic supercell containing 32 Pd atoms. In Table SI the tunneling rates with varying number of beads is presented. We analyze the PT/T_c ratio where P is the number of beads, T the temperature and T_c the cross-over temperature as suggested in Ref.[1]. We also report the T_c for H and D in tables SII and SIII. It can be seen that for all the temperatures considered, PT/T_c ratios of 36 and 72 deliver converged rates within 10% and 2%, respectively.

T(K)	T/T_c	P	PT/T_c	k_{inst} (s^{-1})
125	0.92	32	29.4	3.17
125	0.92	96	88	3.66
115	0.85	32	27.2	6.44(-1)
115	0.85	64	54.4	5.50(-1)
115	0.85	96	82	5.38(-1)
115	0.85	128	108	5.34(-1)
115	0.85	256	216	5.39(-1)
102	0.75	48	36	4.74(-2)
102	0.75	96	72	4.39(-2)
102	0.75	128	96	4.33(-2)
82	0.60	64	38	1.55(-4)
82	0.60	128	76	1.41(-4)
82	0.60	160	96	1.40(-4)
68	0.50	72	36	3.04(-7)
68	0.50	144	72	2.87(-7)
68	0.50	192	96	2.85(-7)

TABLE SI: Tunneling Rates for $Pd_{04}H$.

System	T_c (K)	ω_{TS} (cm^{-1})
$Pd_{04}H$	136	594
$Pd_{16}H$	123	537
$Pd_{32}H$	114	502

TABLE SII: Cross-over temperature (T_c) and imaginary frequency at the transition state (ω_{TS}). $Pd_{32}H$, $Pd_{16}H$, and $Pd_{04}H$, were computed with a k-grid mesh of 6x6x6, 6x6x6, and 12x12x12, respectively.

System	T_c (K)	ω_{TS} (cm^{-1})
$Pd_{04}D$	96	422
$Pd_{16}D$	87	381
$Pd_{32}D$	82	356

TABLE SIII: Cross-over temperature (T_c) and imaginary frequency at the transition state (ω_{TS}). $Pd_{32}D$, $Pd_{16}D$ and $Pd_{04}D$, were computed with a k-grid mesh of 6x6x6, 6x6x6, and 12x12x12, respectively.

II. MCTDH CALCULATIONS

A. Flux-side approach

The thermal rate constant k_β of the isomerization reaction A $\rightleftharpoons$ B is traditionally expressed as the long time limit of a time-dependent "rate constant" $k_\beta(t)$, $k_\beta = \lim_{t\to\infty} k_\beta(t)$[2–4]. The latter involves the so-called flux-side correlation function $C^\beta_{\rm fs}(t)$ and, in its refined (improved) form[5], reads as

$$k_\beta(t) = \frac{1}{Z_A}\frac{C^\beta_{\rm fs}(t)}{P_A(0) + [P_A(0)-1]\,\chi_\beta - \left(\frac{1}{Z_A}+\frac{1}{Z_B}\right)\int_0^t C^\beta_{\rm fs}(\tau)d\tau}. \tag{1}$$

Here, h is the projection operator that separates the configuration space of the products from that of the reagents, Z_A and Z_B are, respectively, the reagent and product partition functions,

$$Z_A = {\rm Tr}\left(e^{-\beta H}\,(1-h)\right) \quad Z_B = {\rm Tr}\left(e^{-\beta H}h\right)$$

$\chi_\beta = Z_A/Z_B$ is the inverse equilibrium constant of the reaction, $P_A(0)$ is the initial population of the reactants' well

$$P_A(0) = 1 - \frac{1}{Z_A}{\rm Tr}\left(e^{-\beta H/2}\,(1-h)\,e^{-\beta H/2}h\right)$$

and

$$C^\beta_{\rm fs}(t) = {\rm Tr}\left(F_\beta h(t)\right) \tag{2}$$

is the above mentioned flux-side correlation function in its most popular, symmetrized form[3]. The latter is the key quantity and requires, besides h above, the Boltzmannized flux operator

$$F_\beta = e^{-\beta H/2}Fe^{-\beta H/2} \quad F = \frac{i}{\hbar}[H,h] \tag{3}$$

which is the Boltzmannized version of the Heisenberg time derivative of h (*i.e.*, the flux operator F). In Eq. 1 the long time limit is the true infinite time limit (*i.e.*, the notation $t\to\infty$ is exact, with no *caveats*), although in practice the appropriate t is a macroscopically small time beyond which $k_\beta(t)$ approaches a constant value. Since most often it holds

$$P_A(0) \approx 1 \text{ and } \quad \int_0^{t_P} C_{\rm fs}(\tau)d\tau \ll \frac{Z_A Z_B}{Z_A+Z_B},$$

the rate takes the form

$$k_\beta \approx \frac{1}{Z_A}\,{}_{"}\lim_{t\to\infty}{}_{"}\, C_{\rm fs}(t) \tag{4}$$

where now the limit needs to be interpreted at the *plateau* time t_P where the correlation function attains a constant value. Eq. 4 represents the celebrated "flux-side" expression of the thermal rate constant. For a derivation of Eq. 1 appropriate to a condensed-phase environment see Ref. 6.

B. Boltzmann sampling

We focus here on practical issues that arise when numerically evaluating the trace expressions of Eq. 2 for a condensed-phase problem involving many degrees of freedom[7,8]. In particular, we describe the importance sampling scheme introduced by the authors of Ref.s 7 and 8 to turn the problem into an efficient Monte Carlo sampling of the state space. We shall first describe such 'Monte Carlo wavepacket strategy' for computing average values of observables and, later, highlight the amendments needed to evaluate the correlation functions.

In the following we assume that H takes the form $H = H_S + H_{\rm int} + H_B$ where H_S is the system Hamiltonian, H_B is a sum of independent oscillator Hamiltonians and $H_{\rm int}$ the interaction term between the system and the bath. Accordingly, for the state space we have $\mathcal{H} = \mathcal{H}_S \otimes \mathcal{H}_B$, and we make use of vectors of the form $|n, N\rangle \equiv |n\rangle\,|N\rangle$ where $|n\rangle$ is an arbitrary system state and $|N\rangle$ an eigenstate of the bath, i.e., for $N = \{n_1 n_2 .. n_k ...\}$,

$$H_B\,|N\rangle = E_N\,|N\rangle \quad \text{and} \quad E_N = \sum_k \hbar\omega_k \left(n_k + \frac{1}{2}\right).$$

1. Averages of observables

The equilibrium average value of an operator A takes the form

$$\langle A\rangle = \frac{1}{Z}{\rm Tr}(e^{-\beta H}A) \equiv \frac{1}{Z}{\rm Tr}(e^{-\frac{\beta}{2}H}Ae^{-\frac{\beta}{2}H}) = \frac{1}{Z}\sum_{n,N}\langle\Psi^{\beta}_{n,N}|A|\Psi^{\beta}_{n,N}\rangle$$

where $|\Psi^{\beta}_{n,N}\rangle = e^{-\frac{\beta}{2}H}\,|n, N\rangle$. This equation is best re-written in terms of *normalized* vectors $|\Phi^{\beta}_{n,N}\rangle$, which are those directly available from the MCTDH package upon imaginary-time evolution. Clearly, for a solution of the Bloch equation

$$-\frac{\partial\,|\Psi_\beta\rangle}{\partial\beta} = H\,|\Psi\rangle \quad |\Psi_{\beta=0}\rangle = |\Psi_0\rangle$$

given its squared norm $p(\beta) = \langle\Psi_\beta|\Psi_\beta\rangle$ and the energy expectation $\epsilon(\beta) = \langle\Psi_\beta|H|\Psi_\beta\rangle / p(\beta)$, we have $\frac{\partial p}{\partial \beta}(\beta) = -2\epsilon(\beta)p(\beta)$, hence $p\,(\beta) = e^{-2\int_0^\beta \epsilon(\tau)d\tau}$ and $|\Psi_\beta\rangle = e^{-\int_0^\beta \epsilon(\tau)d\tau}\,|\Phi_\beta\rangle$. Thus,

$$\begin{aligned}\langle A\rangle &= \frac{1}{Z}\sum_{n,N} p_{n,N}\left(\frac{\beta}{2}\right)\langle\Phi^\beta_{n,N}|A|\Phi^\beta_{n,N}\rangle \\ &= \frac{Z_0}{Z}\sum_N \frac{e^{-\beta E_N}}{Z_0}\sum_n W_{n,N}(\beta)\,\langle A\rangle^\beta_{n,N}\end{aligned}$$

where Z_0 is the partition function of the uncoupled bath, $\langle A\rangle^\beta_{n,N} = \langle\Phi^\beta_{n,N}|A|\Phi^\beta_{n,N}\rangle$ are expectation values and

$$W_{n,N}(\beta) = e^{+\beta E_N} e^{-2\int_0^{\beta/2}\epsilon_{n,N}(\tau)d\tau} \tag{5}$$

are thermal factors determined by the average energy $\epsilon_{n,N}(\tau)$ of the state $|\Phi^\tau_{n,N}\rangle$ during the imaginary-time evolution. The ensemble-average takes thus the form of a Boltzmann-weighted sum of terms which can be efficiently evaluated *via* Monte Carlo sampling,

$$\langle A\rangle = \frac{Z_0}{Z}\sum_n \langle\langle W_{n,N}(\beta)\,\langle A\rangle^\beta_{n,N}\rangle\rangle \tag{6}$$

where the double bracket denotes the Boltzmann average (and N is the corresponding random variable). This expression can be further rewritten upon noticing that $Z = Z_0\sum_n\langle\langle\ W_{n,N}(\beta)\ \rangle\rangle$ (as it follows from Eq. 6 upon setting $A = 1$), hence

$$\langle A\rangle = \frac{\sum_n\langle\langle\ W_{n,N}(\beta)\,\langle A\rangle^\beta_{n,N}\rangle\rangle}{\sum_n\langle\langle\ W_{n,N}(\beta)\rangle\rangle} \tag{7}$$

which requires just one sampling.

In practice, given a basis of $\mathcal{H}_S$ a number of bath configurations $|N_i\rangle$ are generated from the Boltzmann distribution and the vectors $|n, N_i\rangle$ are propagated in imaginary-time to compute the expectation values and the thermal factors. Sampling can be performed independently for each bath oscillator, using the known cumulative distributions $P_\nu = \sum_{k=0}^\nu \rho_k$ (where ρ_k are the Boltzmann probabilities) of a harmonic oscillator with frequency ω,

$$P_\nu = 1 - e^{-\beta\hbar\omega(\nu+1)}.$$

That is, $\nu_i = \mathrm{int}(-\ln(\xi_i/\beta\hbar\omega))$, for ξ_i random in $[0,1]$, gives a set of quantum numbers ν_i Boltzmann distributed. Thus, besides bookkeeping issues, the procedure is entirely straightforward and generates vectors $|N_I\rangle \equiv |n_{i_1}\rangle\,|n_{i_2}\rangle\,..\,|n_{i_k}\rangle\,..\,|n_{i_F}\rangle$ where $I = (i_1 i_2..i_k..i_F)$ and F

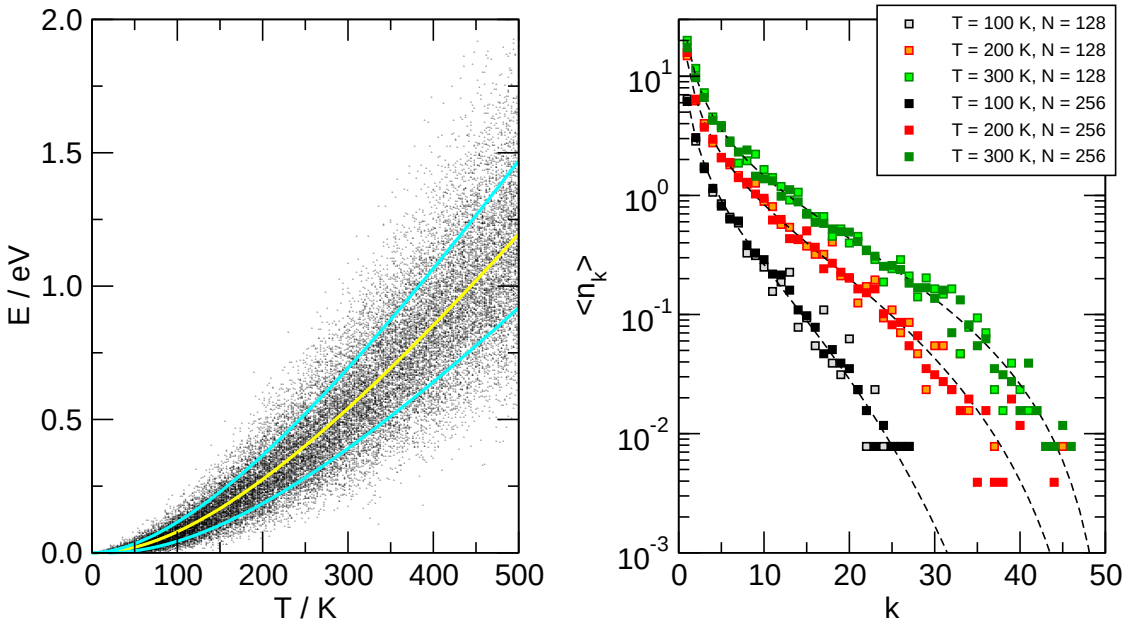

FIG. S1: Sampling of the bath (results for a typical bath containing $F = 50$ oscillators). Left: individual energy of the bath states $|N_I\rangle$ sampled at different temperatures ($N_{\rm MC} = 128$ realizations for clarity), along with the theoretical mean energy $\langle E\rangle$ (yellow) and $\langle E\rangle \pm \Delta E$ (cyan), where ΔE^2 is the energy variance. Right: average occupation numbers n_k obtained for $N_{\rm MC} = 128, 256$ realization, compared with the exact results (dashed lines).

is the number of bath degrees of freedom. Fig. S1 illustrates typical results of such sampling for the case considered in the main text, which used $F = 50$ harmonic oscillators with frequencies

$$\omega_k = -\omega_c \ln\left(\frac{k}{F+1}\right)$$

where ω_c is a cutoff frequency. This is a widely used discretization of the Ohmic bath with exponential cutoff, $J(\omega) = m\gamma\omega e^{-\omega/\omega_c}$, provided the couplings c_k with the system coordinate are set according to

$$c_k = \omega_k \sqrt{\frac{2}{\pi}\frac{m\gamma\omega_c}{F+1}M}$$

where m and M are, respectively, the system and the oscillators mass, and γ is the damping coefficient ($\gamma = \tilde{\eta}_0/m$, with $\tilde{\eta}_0$ being the static friction coefficient as defined in the main text.). Here, the cutoff frequency was set to $\omega_c = 500$ cm^{-1}.

Importantly, we notice that the reagent partition function takes a form similar to the

total partition function

$$Z_A = Z_0 \sum_n \langle\langle\ W_{n,N}(\beta)\, \langle h_A \rangle^{\beta}_{n,N}\ \rangle\rangle \tag{8}$$

but now the system states are better chosen to closely resemble "the reagent states" since, in practice, a quickly convergent sum over n is highly desirable. In our implementation they are eigenstates of a fictitious Hamiltonian that describes reagents only, *i.e.* the states $|n\rangle$ are chosen to be eigenstates of $\tilde{H}_S = \frac{p^2}{2m} + \tilde{v}$ where $\tilde{v}$ is a modified potential with the "reaction channel artificially closed". This choice improves much the Monte Carlo convergence and, in practice, requires 1-2 system states (depending on the temperature) to obtain a numerically converged value of the reagent partition function. Notice further that the convergence depends also on other numerical parameters. For instance, a grid for the bath oscillations that is "centered" around the classical equilibrium position (the reagent minimum of the potential) is much more efficient that an "unbiased" grid (like the one appropriate for the flux evaluation). That is, for the typical Hamiltonian

$$H = H_S + \sum_k \left[\frac{p_k^2}{2M} + \frac{M\omega_k^2}{2} \left(x_k - \frac{c_k s}{M\omega_k^2} \right)^2 \right]$$

the center of the grid for the k^{th} harmonic oscillator is better placed at

$$x^{\ominus} = \frac{c_k}{M\omega_k^2} s_{\min}$$

where $s_{\min}$ is the value of the system coordinate at the bottom of the reagent well.

2. Flux-side correlation

The standard flux-side correlation $C^{\beta}_{\text{fs}} \equiv \text{Tr}(e^{-\frac{\beta}{2}H} F e^{-\frac{\beta}{2}H} h(t))$ can be evaluated similarly to the expectation values considered above by introducing the spectral representation of $F = \sum_u u\, |u\rangle\, \langle u|$ and re-writing the trace as a sum over states

$$C^{\beta}_{\text{fs}}(t) = \sum_u \sum_N u\, \langle uN|h(\tau)|uN\rangle$$

where the expectation of the operator $h(\tau) = e^{\frac{i}{\hbar}H\tau^*} h e^{-\frac{i}{\hbar}H\tau}$ (with $\tau = t - i\frac{\hbar\beta}{2}$) requires both the imaginary and the real time evolution. This general procedure is, however, numerically inconvenient since F (albeit *system-only*) has many contributing eigenstates, thereby making the sum over u rather long[9]. Fortunately, at least for the case we are interested in, there is

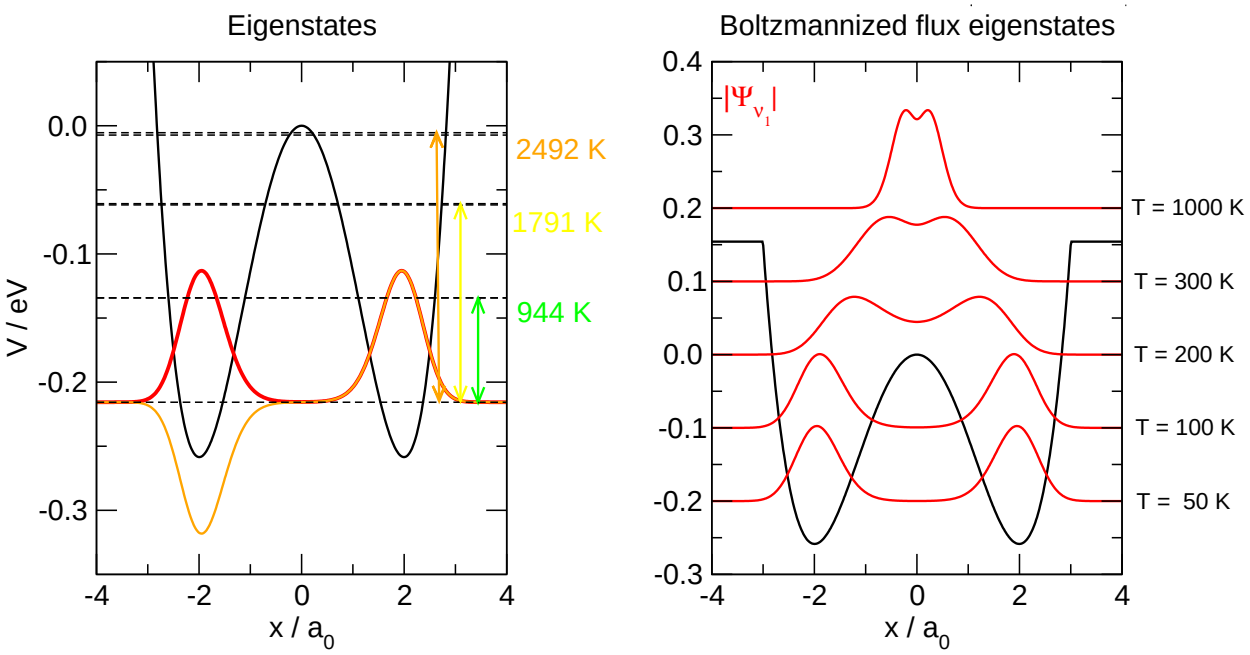

FIG. S2: Boltmannized flux eigenstates $|\nu_\beta\rangle$ for a symmetric double well potential (black curves). Left: the two lowest-lying energy eigenstates forming the ground-state tunneling-split doublet. Right: the absolute value of the Boltzmannized-flux eigenfunction with the largest positive eigenvalue, as obtained at the indicated temperatures (vertically shifted for clarity). a_0 refers to the Bohr radius.

a way out of this "dimensionality" problem: the *Boltzmannized* flux operator is intrinsically of low-rank, that is it reads as

$$F_\beta^S = e^{-\frac{\beta}{2}H_S} F e^{-\frac{\beta}{2}H_S} = \sum_\nu \nu(\beta)\, |\nu_\beta\rangle \langle\nu_\beta|$$

where only few values of $\nu(\beta)$'s are significant (in fact just two, related to each other by time inversion, if the temperature is low enough, as it easily follows by the two-state approximation of the dynamics)[10]. Fig. S2 illustrates the typical behavior of the most important flux eigenstates at varying temperatures, and their relation to the energy eigenstates. To exploit the above property, following Craig *et al.* [6], we write

$$\begin{aligned} F &= e^{+\frac{\beta}{2}H_S} F_\beta^S e^{+\frac{\beta}{2}H_S} = \sum_\nu \nu(\beta) e^{+\frac{\beta}{2}H_S} |\nu_\beta\rangle \langle\nu_\beta| e^{+\frac{\beta}{2}H_S} \\ &\equiv \sum_\nu w_\nu(\beta)\, |\bar\nu_\beta\rangle \langle\bar\nu_\beta| \end{aligned}$$

where $|\bar{\nu}_\beta\rangle$ are normalized, imaginary-time backward-propagated flux eigenvectors,

$$|\bar{\nu}_\beta\rangle = \frac{1}{\sqrt{\langle\nu_\beta|e^{\beta H_S}|\nu_\beta\rangle}} e^{\beta H_S/2}\,|\nu\rangle$$

and $w_\nu(\beta) = \nu(\beta)\,\langle\nu_\beta|e^{\beta H_S}|\nu_\beta\rangle$ are flux-weights. The $|\bar{\nu}_\beta\rangle$'s are non-orthogonal, yet rather useful since they provide a compact representation of the flux operator. With these definitions, we have

$$\begin{aligned} C_{\rm fs}^\beta &= \sum_\nu \mathrm{Tr}\left(e^{-\beta H/2}\,|\bar{\nu}_\beta\rangle\,\langle\bar{\nu}_\beta|\,e^{-\beta H/2}h(t)\right) w_\nu(\beta) \\ &\equiv \sum_\nu \sum_N w_\nu(\beta)\,\langle\bar{\nu}_\beta N|e^{-\beta H/2}h(t)e^{-\beta H/2}|\bar{\nu}_\beta N\rangle \end{aligned}$$

and everything proceeds as above. Specifically, introducing the normalized vectors

$$|\Phi_{\nu,N}^\beta\rangle = \frac{1}{\sqrt{p_{\nu N}(\beta)}} e^{-\beta H/2}\,|\bar{\nu}_S N\rangle \;\;, \qquad p_{\nu N}(\beta) = e^{-2\int_0^{\beta/2}\epsilon_{\nu N}(\tau)d\tau},$$

their real-time evolutions

$$|\Phi_{\nu,N}^\beta(t)\rangle = e^{-\frac{i}{\hbar}Ht}\,|\Phi_{\nu,N}^\beta\rangle$$

and the expectation $\langle h(t)\rangle_{\nu N}^\beta = \langle\Phi_{\nu,N}^\beta(t)|h|\Phi_{\nu,N}^\beta(t)\rangle$ we write

$$C_{\rm fs}^\beta = Z_0 \sum_N \frac{e^{-\beta E_N}}{Z_0} \sum_\nu w_\nu(\beta) W_{\nu N}(\beta)\,\langle h(t)\rangle_{\nu N}^\beta\,,$$

where $W_{\nu N}(\beta) = p_{\nu N}(\beta)e^{\beta E_N}$ are thermal factors (Eq. 5) and $w_\nu(\beta)$ are (thermal) flux weights. Equivalently,

$$C_{\rm fs}(t) = Z_0 \sum_\nu \langle\langle\; w_\nu(\beta) W_{\nu N}(\beta)\,\langle h(t)\rangle_{\nu N}^\beta\rangle\rangle \tag{9}$$

is the working expression involving

(i-a) a "system" preparation to define the appropriate system states $|\bar{\nu}_\beta\rangle$,

(i-b) a Monte Carlo sampling of the (uncoupled) bath state, which delivers bath states $|N\rangle$,

(ii) a relaxation dynamics with the full Hamiltonian H for each state $|\bar{\nu}_\beta N\rangle$

(iii) a real time dynamics with the same Hamiltonian on the relaxed states obtained in *(ii)*.

When combined with the calculation of the reagent partition function, Eq. 8, this recipe gives the thermal rate constant of Eq. 4 or, with minor additional effort, the one defined by Eq. 1.

In closing this section it is worth noticing that the manipulations above with the Boltzmann operator are well defined when the Hamiltonian operator H_S is bound[11] but some regularization is needed when — as it is often the case in realistic problems — the spectrum of H_S is unbound. This is particularly important for numerical applications because the presence of high-lying energy eigenstates makes $\exp(-\beta H_S)$ nearly singular and $\exp(+\beta H_S)$ numerically unstable, increasingly so when reducing the temperature ($\beta \to \infty$). Fortunately, such high-lying energy eigenstates should not play any role in the dynamics (particularly at the low temperatures where a quantum description is required) and the simple regularization of replacing H_S with its projection $\bar{H}_S$ on a low-lying energy eigenspace suffices. Specifically, defining P_n the projection onto the first (lowest lying) n eigenstates of H_S one defines $\bar{H}_S = P_n H_S P_n$ and uses it in place of H_S in some of the expressions above. This is entirely legitimate since the aim is just to re-write F in a suitable way, but of course one must ensure that $\bar{H}_S$ closely resembles H_S for the expansion to be compact. In practice, then, one uses H_S to define the Boltzmannized flux and diagonalize it, and then switches to $\bar{H}_S$ when propagating backward in imaginary time, making sure that the "error" is kept below a desired threshold[12,13].

C. ML-MCTDH wavefunction and calculation setup

Fig. S3 shows the tree structure defining the ML-MCTDH wavefunction. It was obtained after extensive testing, and found to accurately reproduce previous ML-MCTDH and PI results, at both high and low temperatures at varying coupling strengths, ranging from the weak to the strong coupling limits. The number of logical modes used in each layer was kept small ($2-3$) and each of them was described with several single-particle functions ($12-6$). Only in the bottom layer, depending on the size of the primitive grids, the bath degrees of freedom (the "q_k"s in Fig. S3, sorted in order of increasing frequency) were grouped in $3-4$ dimensional single-particles. The system mode (the "x" in Fig. S3) is located in the group of bath modes with comparable frequency, although described separately from the bath modes and with the help of a large number of SPFs. As for the primitive grids we

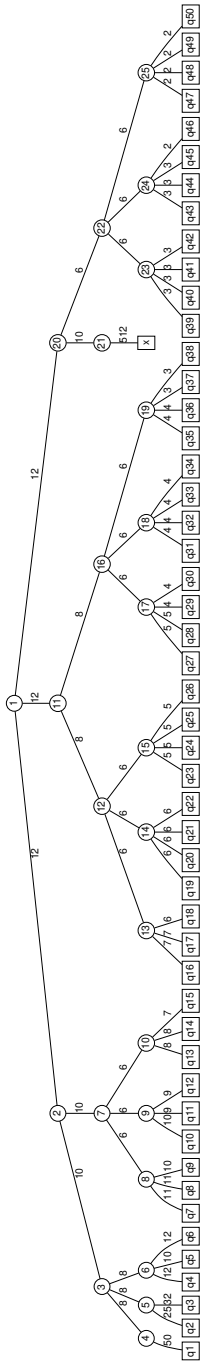

FIG. S3: Adopted tree structure for the ML-MCTDH wavefunction. Each circle denotes a MCTDH-like expansion in the tree, along with its modes (the arms) and the number of the single particle functions used in the expansion (the numbers on the arms). Squares denote the bottom layers where modes reduce to physical degrees of freedom and the numbers represent the size of the primitive grids. Here x is the system coordinate and the q_k's are bath coordinates.

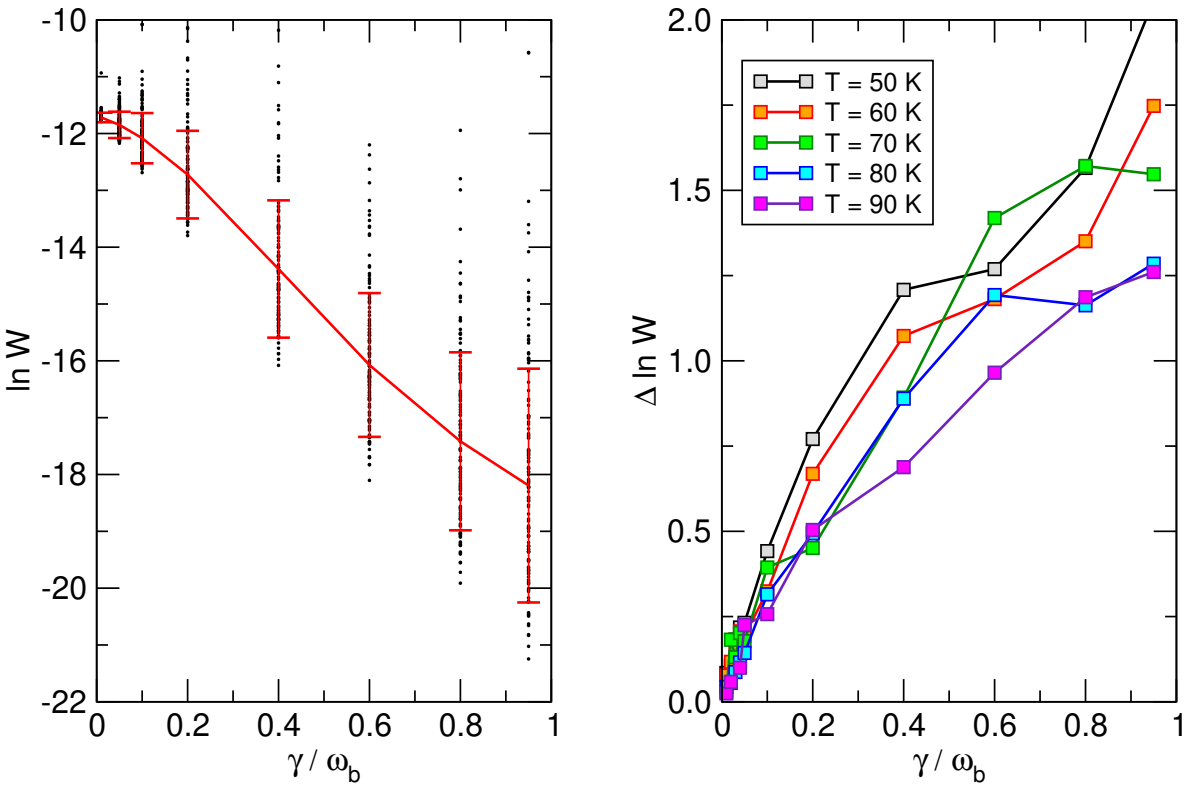

FIG. S4: Behavior of the thermal factors otained in thermalization step. Left: individual realizations, with their average and root mean square given as red curve with error bars. Right: root mean square for different temperatures, as a function of the coupling strength.

used Harmonic Oscillator - Discrete Value Representation (HO-DVR) grids for each bath degrees of freedom, which amounts to introduce a phonon basis of the same size for the corresponding mode. The grids for the low frequency modes used several tens of points (as indicated in Fig. S3), and were extended if necessary to accommodate each realization sampled from the canonical ensemble of the bath. The grids for the high-frequency modes, on the other hand, used much fewer grid points since they were barely excited during the dynamics. The system degree of freedom was described with a uniformly spaced grid, a Fast Fourier Transform - Discrete Value Representation (FFT-DVR), using 512 grid points in the range $x \in [-4, 4]\ a_0$ (with a_0 referring to the Bohr radius).

The MCTDH equations of motion were integrated with the Variable Mean Field scheme, using a variable step-size 8^{th}-order Runge-Kutta integrator for both the amplitude coefficients and the single-particle wavefunctions, and a small accuracy parameter (10^{-8}). The propagation time was set differently according to the coupling strength, in order to guar-

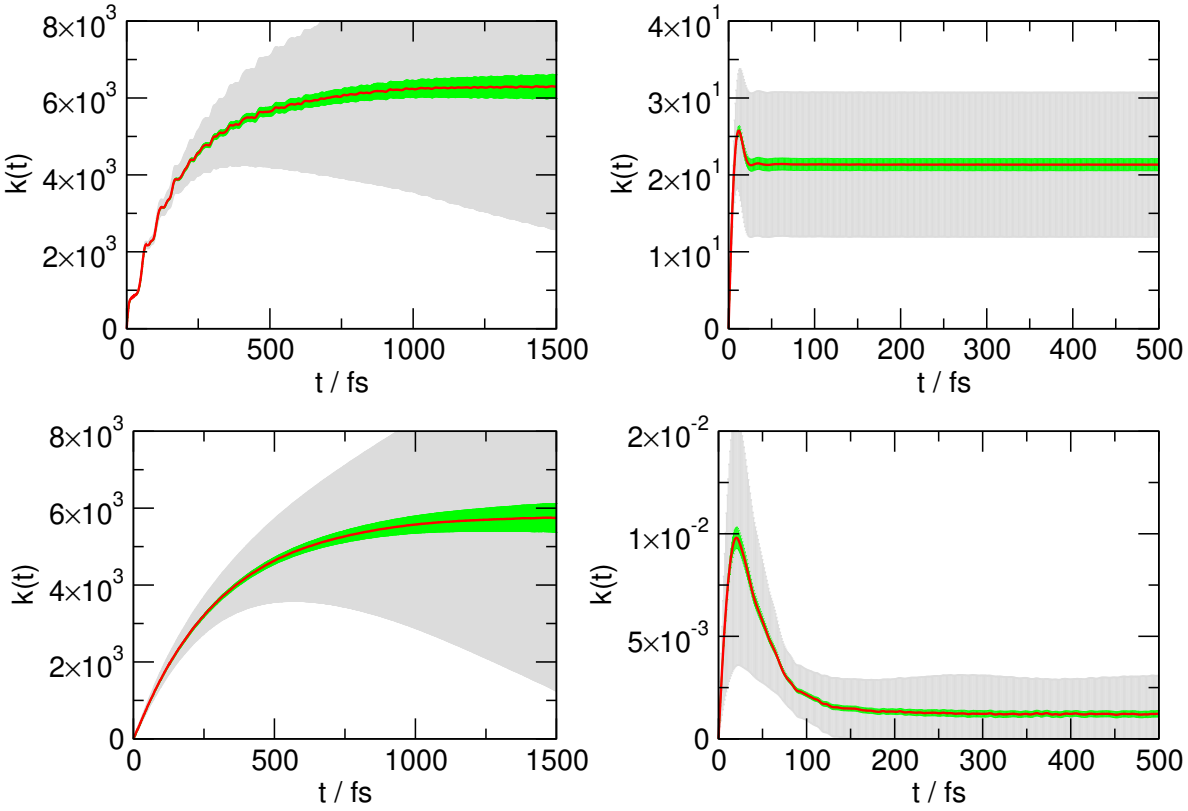

FIG. S5: Illustrative examples showing the behavior of the flux-side correlation function at $T = 90$ K (top row) and $T = 50$ K (bottom row), for very small and large coupling strength, $\gamma/\omega_b = 0.01$ and 0.95, respectively for the left and right panels. Gray (green) area shows the spread (statistical error) calculated as the root-mean-square deviation of x_N (root-mean-square deviation of x_N over square-root of number of realizations).

antee that the computed flux-side correlation functions attained a constant limiting value (which occurs at increasingly longer times when decreasing friction). Similarly, the number of realization was chosen differently depending on the considered temperature and coupling strength, the higher T and/or γ the larger the number of realizations used. Fig. S4 shows the behavior of the thermal factors of Eq. 5 as computed in the "equilibration step" (step ii above), which are the weights with which the individual realizations of the bath enter into the flux-side correlation function expression of Eq. 9 (for a given flux state). Their logarithms are within $0 - 2$ over a wide range of coupling strengths, meaning roughly that each realization has a weight in a two-order-of-magnitude wide interval at most. Fig. S5, on the other hand, displays some illustrative examples of the evolution of the correlation functions, along with the spread of the contributing terms in the sum of Eq. 9. More specifically, the

latter was obtained by grouping results from opposite flux eigenvalues, and rewriting Eq. 9 as an average of individual contributions $x_N = \sum_\nu W_{\nu N}|w_\nu(\beta)| \left[\langle h\rangle_{+|\nu|,N} - \langle h\rangle_{-|\nu|,N}\right]$ with a spread given by the root-mean-square deviation of the x_N's. Hence, provided bath sampling is sufficiently extended, it measures the intrinsic variability of the reaction probability across the thermal equilibrium state.

III. CONVERGENCE TESTS OF DFT CALCULATIONS

A. Energy Barriers

In Fig. S6 the convergence of the energy with respect to k-grid sampling for the hydrogen hopping reaction in Pd is shown. It can be observed that a 6x6x6 k-grid with *light* settings delivers converged results for the reaction energy and energy barrier for the 2x2x2 supercell. The corresponding values obtained for the 1x1x1 supercell show a considerably larger reaction energy and barrier height.

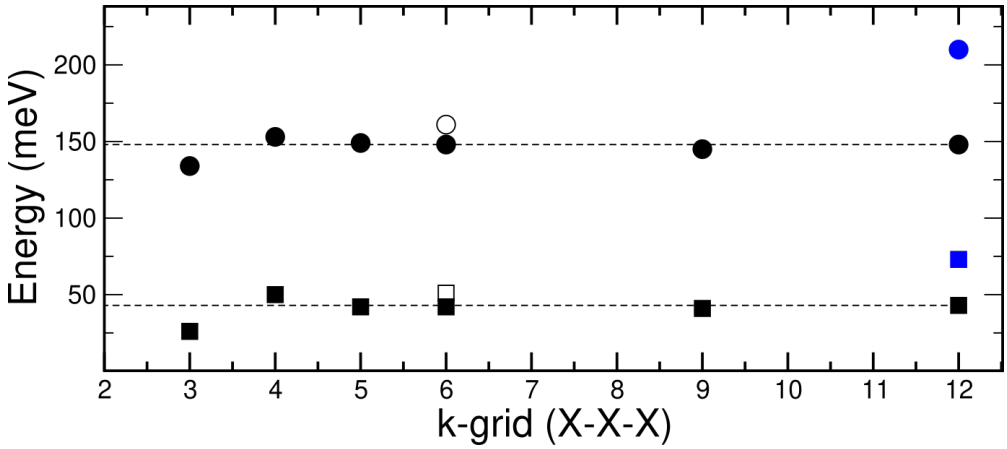

FIG. S6: Reaction energy, $E_\mathrm{T} - E_\mathrm{O}$, and energy barrier heights, $E_\mathrm{SP} - E_\mathrm{O}$, for Pd are represented by squares and circles, respectively. E_T, E_O, and E_SP refer to the potential energy corresponding to structures where the H atom is located at the tetrahedal (T), octahedral (O) and saddle-point (SP) sites, respectively. Values reported without ZPE correction. Calculations were performed using supercells constructed from 2x2x2 (black) and 1x1x1 (blue) copies of the cubic unit cell. Dashed lines are shown as a guide to the eye. Standard *light* with a modified radial multiplier=2 (filled symbols) and *tight* (empty symbols) settings from FHI-aims were used.

B. Friction Calculations

1. k-grid Convergence

Fig. S7 shows the convergence of the friction tensor on the hydrogen on different positions with respect to k-grid sampling. The friction eigenvalues converged within 20 % and 3 % with k-grid of 6x6x6 and 15x15x15, respectively.

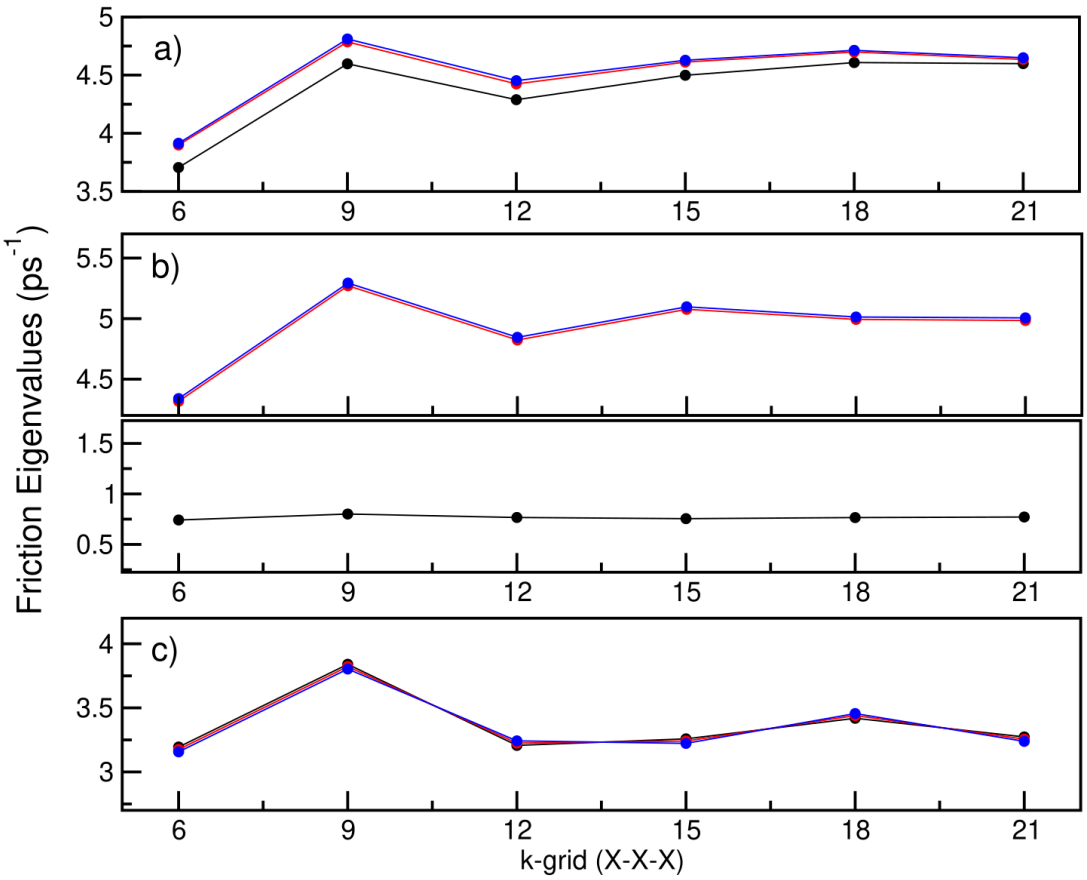

FIG. S7: Convergence of eigenvalues of the friction tensor on the hydrogen atom for $Pd_{32}H$ for a) tetrahedral site, b) transition state between tetrahedral and octahedral sites, and c) octahedral site. Standard *light* from FHI-aims were used with a modified radial multiplier=2 (filled symbols) were used. A broadening of 0.05 eV was used and the reported values are evaluated in the static limit. The different colours represent the three eigenvalues (one unique and two degenerate).

2. Displacement Convergence

Fig. S8 shows the convergence of the friction tensor with respect to the displacement length used in the finite difference calculation. The friction eigenvalues vary by less than 5% in the 0.5×10^{-3} to 4×10^{-3} Å range.

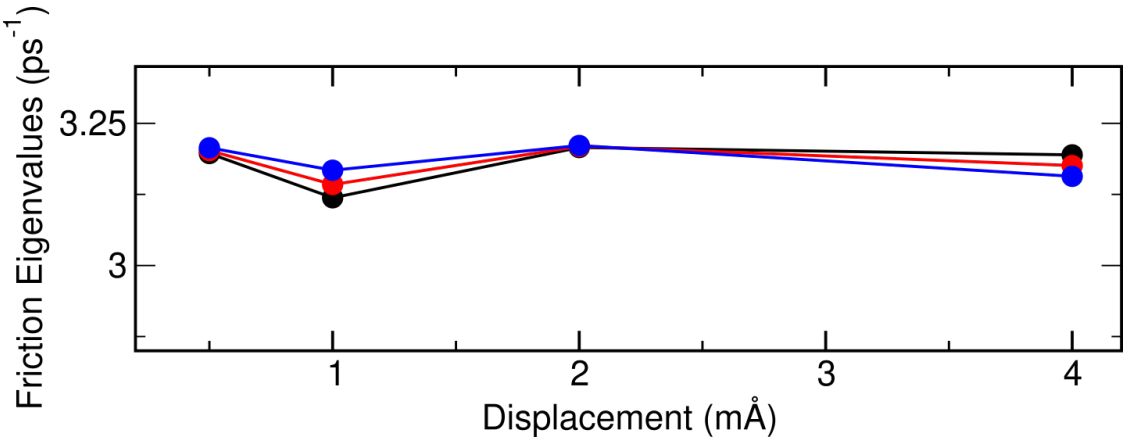

FIG. S8: Convergence of eigenvalues of the friction tensor on the hydrogen atom with respect to displacement length for the hydrogen atom on the octahedral site ($Pd_{32}H$). A k-grid of 6x6x6 has been used and other settings were set equal to the k-grid convergence test.

IV. FRICTION ALONG THE MINIMUM ENERGY PATHWAYS

In Fig. S9-S12, the friction value projected along the minimum energy path together with the minimum energy pathway (MEP) are presented.

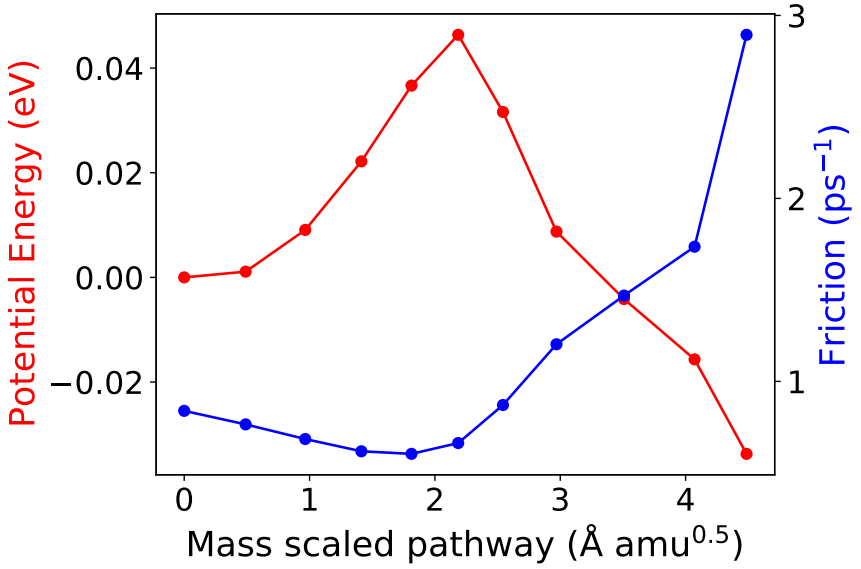

FIG. S9: Electronic friction (Eq. 9 in the main text) and potential energy along the minimum energy pathway for Pt. The former computed only for the hydrogen atom and it is projected along the reaction coordinate. Octahedral→tetrahedral transition is considered.

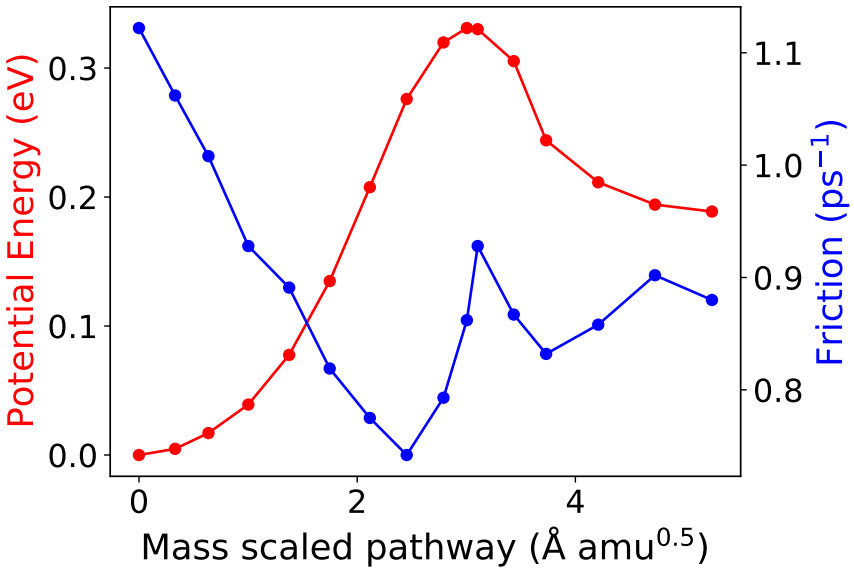

FIG. S10: Same as S9 for Cu.

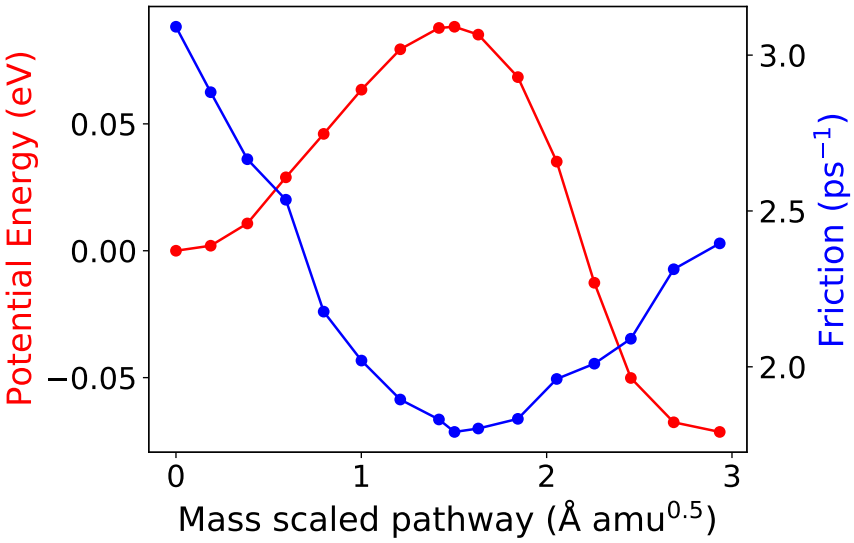

FIG. S11: Same as S9 for Al.

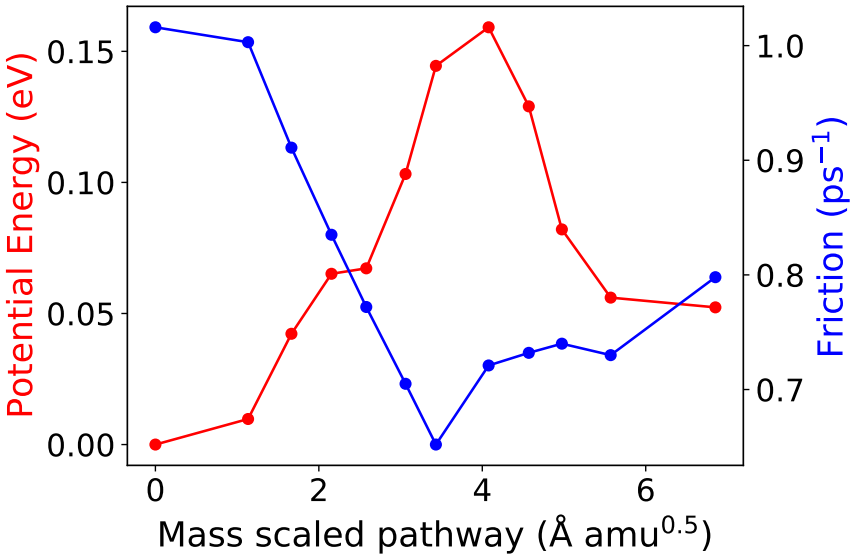

FIG. S12: Same as S9 for Ag.

A. Frequency dependence of Electronic Friction

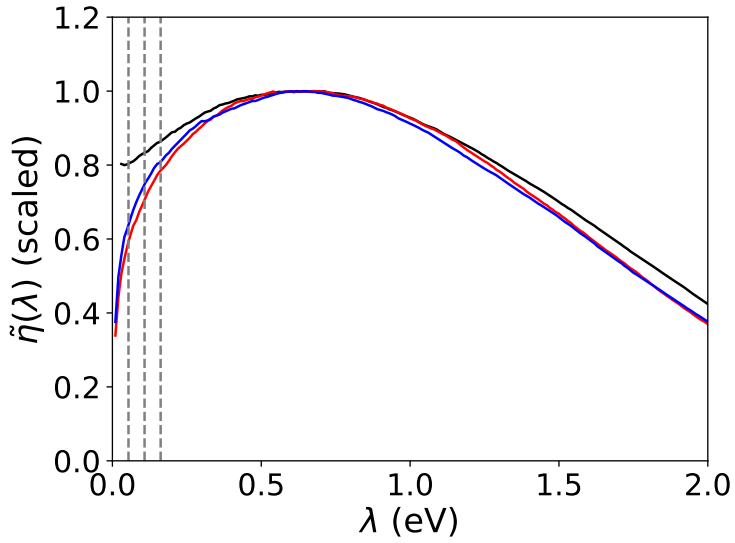

FIG. S13: Frequency dependence of the friction tensor (Eq. 11 in the main text) projected on the reaction coordinate at the reactant (black), transition state (red), and product (blue) states for Pt. The first three non-zero ring-polymer normal modes frequencies at 100K are depicted as vertical dashed gray lines. To ease visual comparison, all curves in panel have been scaled to adopt the value of 1 at the frequency of the first local maximum.

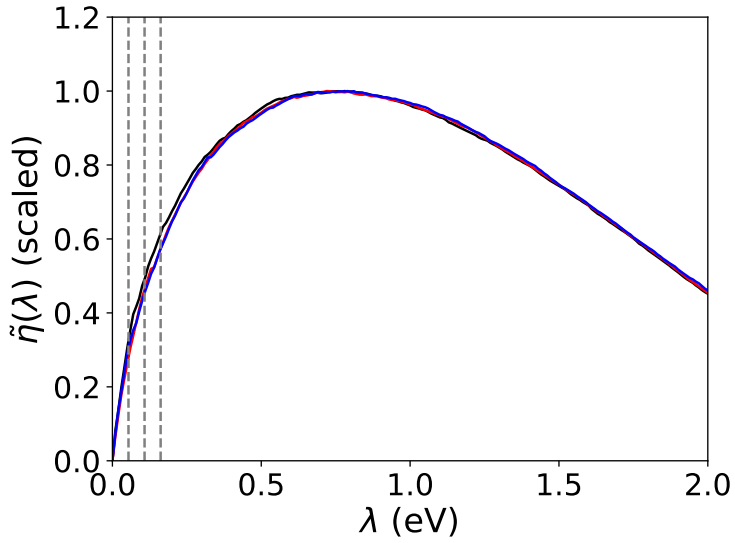

FIG. S14: Same as S13 for Al

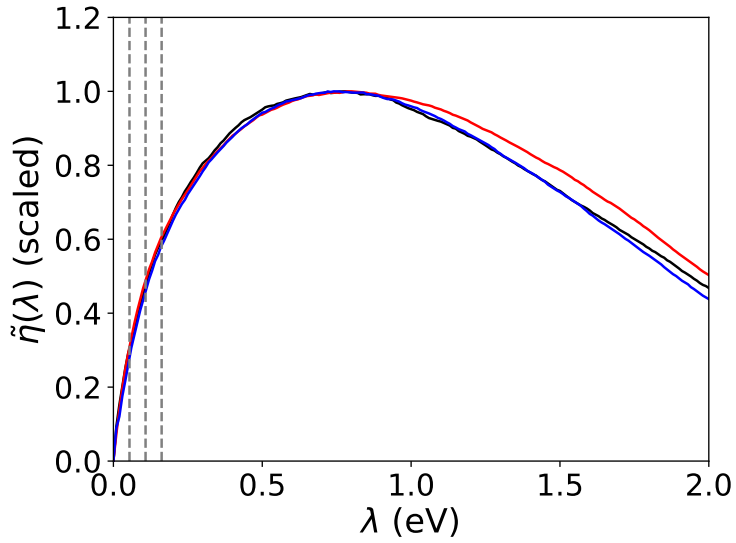

FIG. S15: Same as S13 for Cu

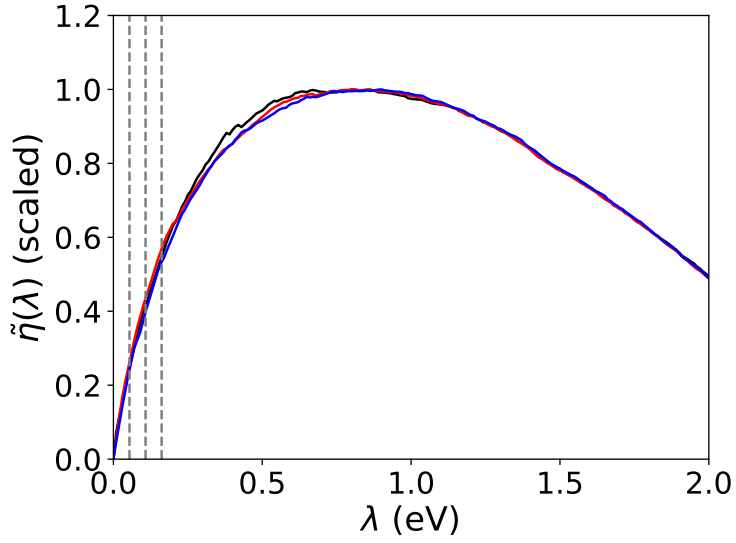

FIG. S16: Same as S13 for Ag

V. ANALYSIS OF PROJECTED DENSITY OF STATES

In Fig. S17 and S18 we show the projected density of states (PDOS) for all the systems considered in this work. These calculations were performed with a 16 $\times$ 16 $\times$ 16 k-point sampling as used for the friction tensor calculations.

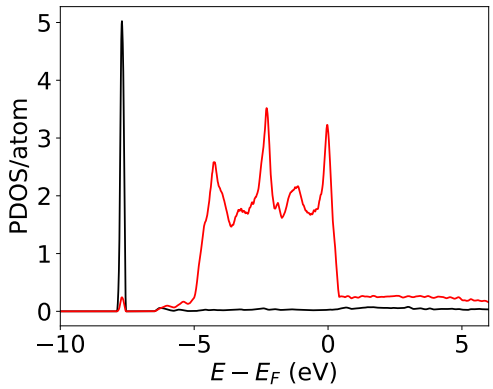

(a) H@Pd reactant geometry

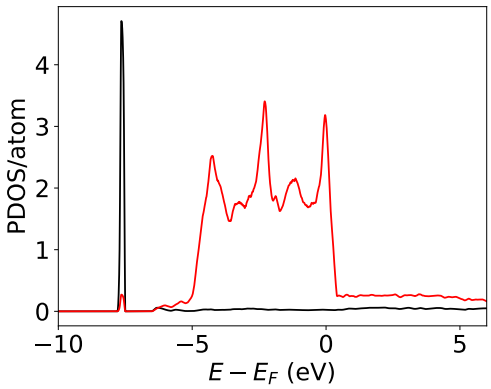

(b) H@Pd transition state geometry

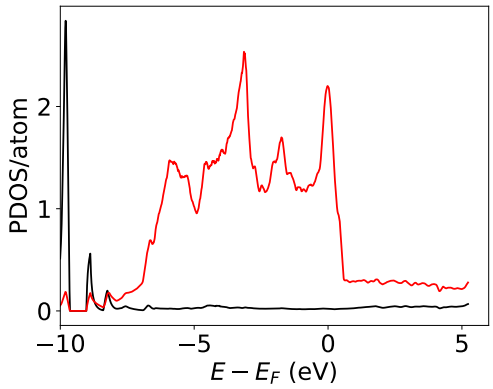

(c) H@Pt reactant geometry

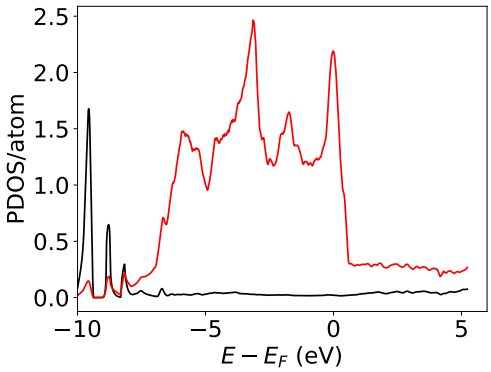

(d) H@Pt transition state geometry

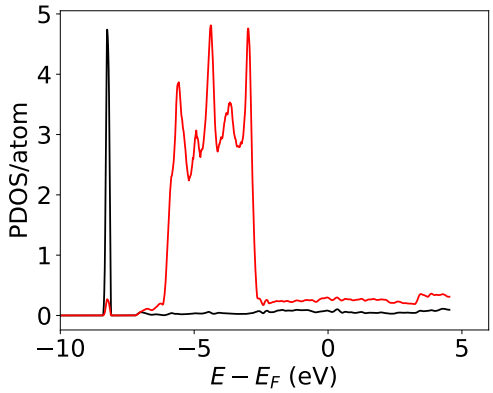

(e) H@Ag reactant geometry

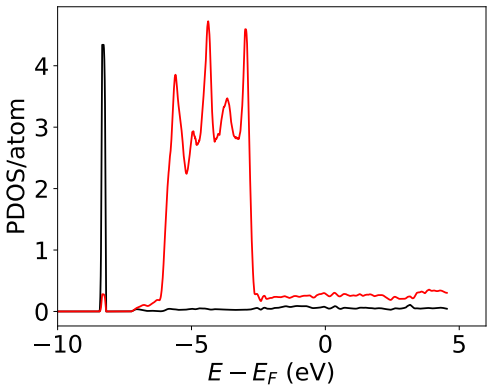

(f) H@Ag transition state geometry

FIG. S17: Projected density of states (PDOS) on H (black) and X (red) atoms for X=Pd, Pt, Ag.

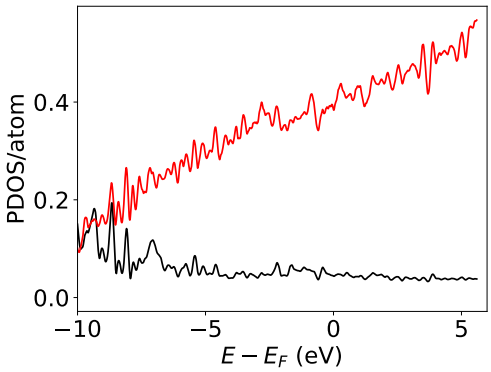

(a) H@Al reactant geometry

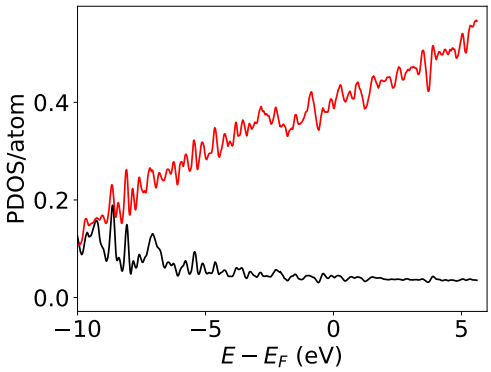

(b) H@Al transition state geometry

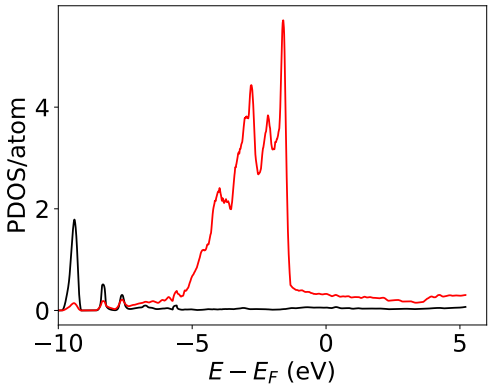

(c) H@Cu reactant geometry

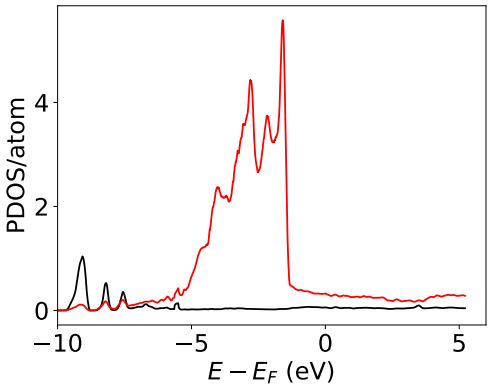

(d) H@Cu transition state geometry

FIG. S18: Projected density of states (PDOS) on H (black) and X (red) atoms for X=Cu, Al

VI. ACCURACY OF RATE ESTIMATION FOR ASYMMETRIC DOUBLE WELL POTENTIAL

Fig. S19 shows the error incurred by the application of the extension of the Grote-Hynes type approximation into the deep tunneling regime an asymmetric double well potential. Similarly to what is observed for a symmetric double well potential in the main text, the error increases with the increase of the friction, the increase of the barrier height, and/or the decrease of the temperature. Except for the highest barrier and friction value at the lowest temperature considered, all the estimated rates are within 1 order of magnitude of the reference values.

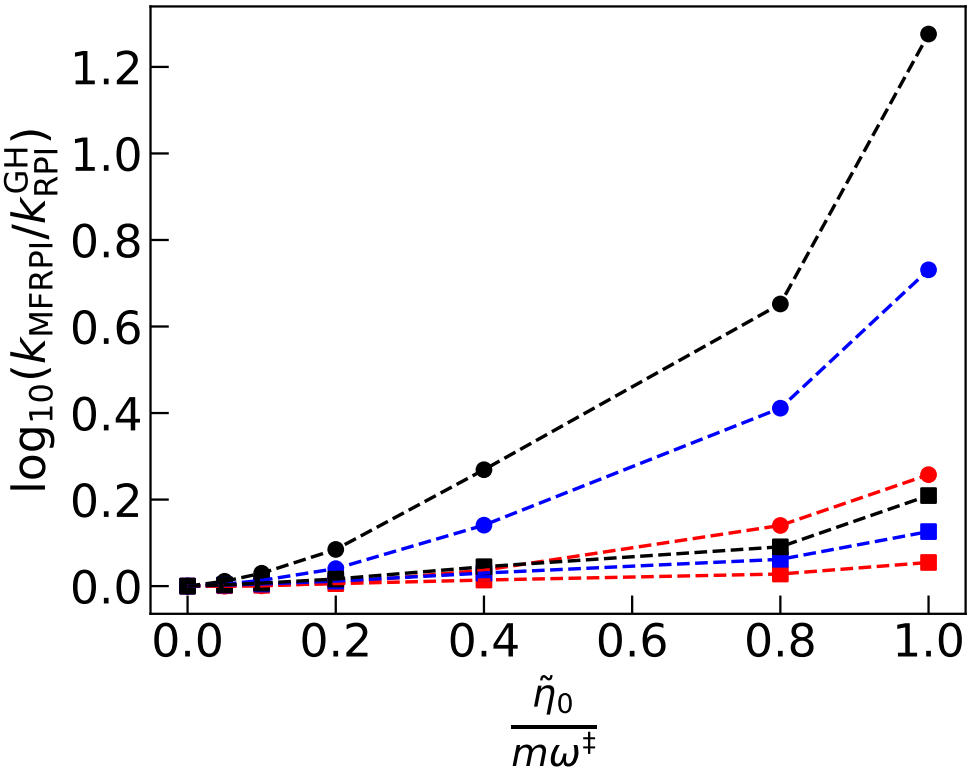

FIG. S19: Error of the RPI rate values obtained by the scaling relation shown in Eq. 13 of the main text ($k_{\mathrm{RPI}}^{\mathrm{GH}}$), compared to the RPI-EF rates (k_{RPIEF}) for an asymmetric double well model (q_0=0.08 Å) at $0.70T_c^\circ$ (squares) and $0.55T_c^\circ$ (circles) for reaction barriers of 258 meV (red), 500 meV (blue), and 1000 meV (black). The error is reported as the ratio of these rates. Analogous plot is presented in main text for a symmetric barrier model.

REFERENCES

[1]Y. Litman, *Tunneling and Zero-Point Energy Effects in Multidimensional Hydrogen Transfer Reactions: From Gas Phase to Adsorption on Metal Surfaces*, Ph.D. thesis, Freie Universität Berlin (2020).

[2]T. Yamamoto, The Journal of Chemical Physics **33**, 281 (1960).

[3]W. H. Miller, S. D. Schwartz, and J. W. Tromp, The Journal of Chemical Physics **79**, 4889 (1983).

[4]W. H. Miller, Journal of Physical Chemistry A **102**, 793 (1998).

[5]A. N. Drozdov and S. C. Tucker, The Journal of Chemical Physics **115**, 9675 (2001).

[6]I. R. Craig, M. Thoss, and H. Wang, J. Chem. Phys. **127**, 144503 (2007).

[7]H. Wang, D. E. Skinner, and M. Thoss, The Journal of Chemical Physics **125**, 174502 (2006).

[8]I. R. Craig, M. Thoss, and H. Wang, Journal of Chemical Physics **127** (2007), 10.1063/1.2772265.

[9]Notice that the total number of wavepackets is given by $M \times N_{\mathrm{MC}}$, where M is number of contributing system states and N_{MC} the size of the Monte Carlo ensemble for the bath, typically $N_{\mathrm{MC}} = 128 - 256$.

[10]Notice that F here is a *system-only* operator and that the above expression is of low rank only in the space of system states $\mathcal{H}_S$: when the same operator is considered in the whole space $\mathcal{H}$ each eigenflux space becomes highly degenerate.

[11]When a maximum eigenvalue exists the Boltzmann operator is non-singular.

[12]The reliability of such regularization can be measured by the difference in the (differently) Boltzmannized flux eigenvalues and by two kinds of errors in the flux eigenstates: there exists a *truncation* error (the distance between the eigenvectors of the differently Boltzmannized operators) and a *propagation* error (defined by back-propagating with the "projected version" of the Boltzmann operator followed by propagation with the true Boltzmann operator). The latter two behave oppositely when varying n since the truncation error determines the quality of the projected Hamiltonian and the propagation error reflects the above mentioned numerical instability.

[13]There is no need for H_S to be the same "system" Hamiltonian appearing in the total Hamiltonian, and one can set it at his own convenience. After all the flux operator F does

not depend on the potential.